

Surface Oxygen Vacancy-Dependent Electrocatalytic Activity of $W_{18}O_{49}$ Nanowires

Huawei Zhou,[†] Yantao Shi,[†] Qingshun Dong,[†] Jian Lin,[‡] Aiqin Wang,[‡] and Tingli Ma^{*,†,§}

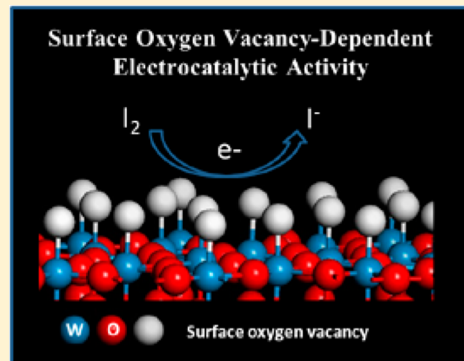
[†]State Key Laboratory of Fine Chemicals, School of Chemistry, Dalian University of Technology, Dalian 116024, China

[‡]State Key Laboratory of Catalysis, Dalian Institute of Chemical Physics, Chinese Academy of Sciences, Dalian 116023, China

[§]Graduate School of Life Science and Systems Engineering, Kyushu Institute of Technology, 2-4 Hibikino, Wakamatsu, Kitakyushu, Fukuoka 808-0196, Japan

Supporting Information

ABSTRACT: Surface oxygen vacancies (SOVs) are the most relevant surface defects in metal oxides (MOs), and they participate in numerous physical and chemical reactions. However, information on the nature, distribution, formation, and reactivity of SOVs, as well as relationships among SOVs, is lacking. Investigating SOVs is difficult because of disturbance by the crystal phase, morphology of bulk materials, and synergistic effect between substrate and catalyst host. Herein, by clarifying the origin of SOVs and their distribution, one-dimensional (1D) tungsten oxide nanowires (NWs) with numerous SOVs were synthesized. Compared with the three-dimensional nanostructure, the high aspect ratio of 1D NW exposed the SOVs on the surface of the nanostructure rather than embedding them in the bulk. To investigate accurately the effect of SOVs on electrocatalytic activity, we clearly identified how SOVs of tungsten oxide catalyst regulate iodide reduction reactions in the solar cell by in situ filling of SOVs in electrodes and maintaining the crystal phase and morphology of NWs. Iodide reduction reaction activity was notably dependent on tungsten oxide catalyst SOVs, which serve as important catalytic site descriptors. These findings may clarify the fundamental features of SOVs on metal oxides and contribute to the rational design of efficient catalysts and supports.



1. INTRODUCTION

The surface of metal oxides (MOs) is important in various applications, including catalysis, sensors, optical and electronic devices, and solar energy technologies.^{1,2} Surface oxygen vacancies (SOVs) are the most relevant surface defects in MOs and participate in numerous physical and chemical reactions.^{3,4} In highly active MO-supported transition metal catalysts, SOVs promote high dispersion and strong anchoring of transition metal nanoparticles on the MO surface. High activity of Au/ceria catalysts has been attributed to highly dispersed Au species that form only in the presence of SOVs.^{5,6} A single-atom catalyst, including isolated single Pt or Ir atoms anchored to the surface vacancies of iron oxide or ceria nanocrystallites, has extremely high atom efficiency and shows excellent stability and high activity for both CO oxidation and preferential oxidation of CO in H_2 .^{7,8} SOVs may assist in band bending and subsequent electron–hole pair separation in photocatalysis of oxides.⁹

Tungsten oxide, an important MO, has been intensively investigated because it possesses distinctive physical and chemical properties.^{10–12} Among them, $W_{18}O_{49}$ is the most investigated and has the largest content of SOVs in $WO_{2.625} - WO_3$. In situ growth of homogeneous subnanometer noble metal on $W_{18}O_{49}$ has been traced back to the high content of SOVs.¹³ Xi et al. reported that SOVs on $W_{18}O_{49}$ participate in

the reduction of carbon dioxide.¹⁴ Our group found that tungsten oxide can supersede noble metal Pt catalysts in solar cells.¹⁵ However, information is lacking on the nature, distribution, formation, and reactivity of SOVs, as well as relationships among SOVs. Investigating SOVs is difficult because of disturbance by the crystal phase, morphology of bulk materials, and synergistic effect between substrate and catalyst host.

Using previous information on the origin of SOVs and their distribution, we synthesized one-dimensional (1D) tungsten oxide nanowires (NWs) with high SOV content. Compared with the three-dimensional (3D) nanostructure, the high aspect ratio of 1D NW expose the SOVs on the surface of the nanostructure rather than embedding them in the bulk. To investigate accurately the effect of SOVs on electrocatalytic activity, we clearly identified how SOVs of tungsten oxide catalyst regulate iodide reduction reactions in the solar cell by in situ filling of SOVs in electrodes and maintaining the crystal phase and morphology of NWs. Surface chemical and electrocatalytic results revealed that iodide reduction activity is notably dependent on the SOVs of tungsten oxide catalysts,

Received: May 4, 2014

Revised: August 5, 2014

which serve as significant catalytic site descriptors. These findings clarify the fundamental features of SOVs on MOs and contribute to the rational design of efficient catalysts and supports.

2. EXPERIMENTAL SECTION

2.1. Synthesis Tungsten Oxide Nanowires. Tungsten oxide NWs were synthesized via the solvothermal utilizing WCl_6 (0.1 g) in ethanol (50 mL) at 180 °C for 24 h.¹⁶ WCl_6 was dissolved in ethanol to form clear yellow solution that was then transferred into a Teflon-lined autoclave. After being heated at 180 °C for 24 h, the mixture was cooled to room temperature naturally. The product was collected by centrifugation and washed repeatedly with water and ethanol, finally followed by vacuum drying at 45 °C overnight.

2.2. Preparation of Catalysts Electrode. W–O_V–W: As-synthesized tungsten oxide powders were dispersed in isopropanol. Then, the obtained suspension was sprayed on fluorine-doped tin oxide (FTO) glass (0.8 cm × 10 cm). The obtained films were sintered in nitrogen atmosphere at 500 °C for 30 min.

W–O–W: In order to prevent disturbance in operation, a half of electrodes in W–O_V–W was cut for oxidation treatment. Then, the cut electrode was transferred to a tube furnace, whose ends are open to air. Filling SOV was carried out at 350 °C for 1 h. Then, the electrodes were cooled to room temperature. By increasing the treatment temperature, the tungsten oxides were converted to WO_3 with light yellow.

2.3. Pt Electrode. The noble metal Pt electrodes were fabricated by pyrolysis of H_2PtCl_6 on FTO glass as previously reported.

2.4. Mediator Preparation for Cyclic Voltammetry. The electrolyte based on I[−]/I₃[−] redox mediator was composed of 0.1 M LiClO₄, 10 mM LiI, and 1 mM I₂ in acetonitrile.

2.5. Solar Cell Fabrication. A layer of 20 nm sized TiO₂ (P25, Degussa, Germany) layer (12 μm) was printed on FTO glass. When the obtained films sintered at 500 °C were cooled to 90 °C, they were immersed in a solution of N719 dye (5×10^{-4} M) in acetonitrile/*tert*-butyl alcohol (1:1 volume ratio) for 22 h. The electrolyte for the solar cell was composed of LiI (0.03 M), 1-butyl-3-methylimidazolium iodide (0.6 M), I₂ (0.03 M), 4-*tert*-butylpyridine (0.5 M), and guanidinium thiocyanate in acetonitrile (0.1 M). The architecture of the dye-sensitized solar cells (DSCs) was assembled by sandwiching electrolyte with a sensitized TiO₂ photoanode and a counter electrode.⁴

2.6. Characterizations. X-ray diffraction (XRD) patterns were obtained using a PANalytical X'Pert diffractometer (Cu K α radiation at $\lambda = 1.54 \text{ \AA}$) sampling at 2°/min, 40 kV, and 100 mA. Nanostructures of our samples were characterized and analyzed by scanning electron microscopy (SEM; Nova Nano SEM 450) and transmission electron microscopy (TEM; FEI Tecnai G2 F30). The film thicknesses were measured using film-thickness measuring device (Surfcom 130A, Japan). X-ray photoelectron spectroscopy (XPS) was carried out in a Thermo ESCALAB 250. Chemisorptions of O₂ were measured using a Micromeritics AutoChem II 2920 instrument with a pulse chemisorption mode. The photocurrent–voltage performance of the DSCs was measured by a Keithley digital source meter (Keithley 2601, USA) equipped with a solar simulator (PEC-L1S, Peccell, Yokohama, Japan). Electrochemical impedance spectroscopy (EIS) experiments were measured in the dummy cells in the dark using a computer-controlled potentiostat (Zennium Zahner, Germany). Tafel polarization measurements

were carried out with an electrochemical workstation system (CHI630, Chenhua, and Shanghai, China) in a symmetrical dummy cell. Effective area of the symmetrical cells in the EIS and Tafel-polarization tests was 0.64 cm².

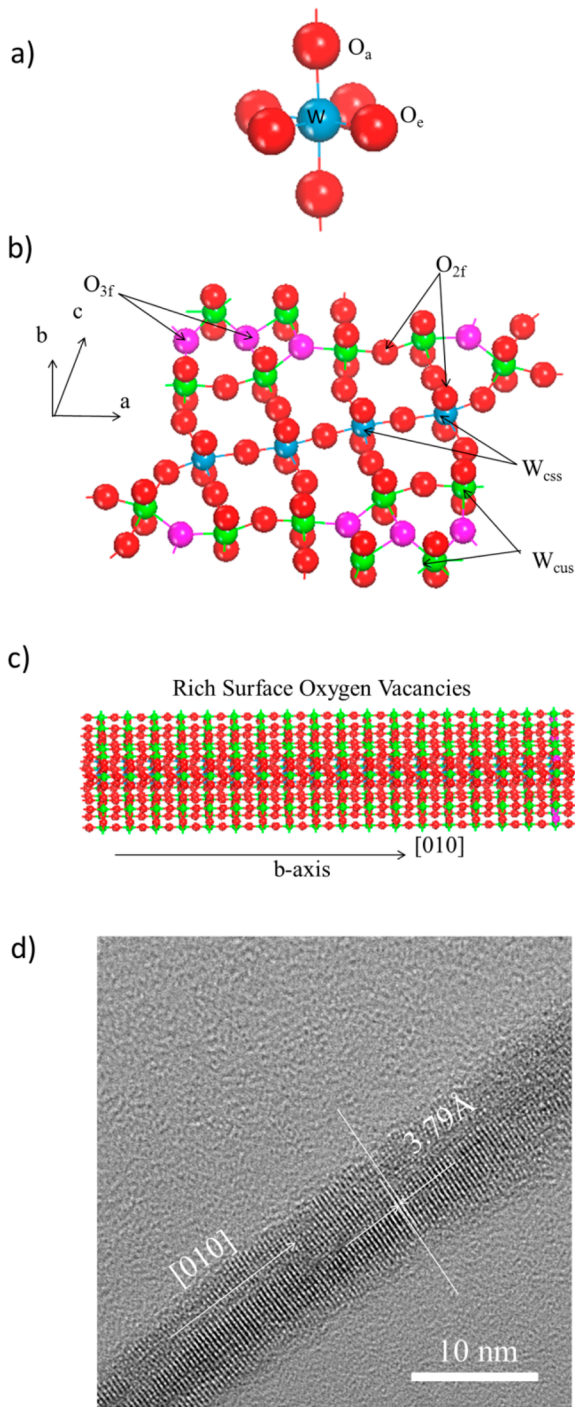
3. RESULTS AND DISCUSSION

The origin of SOVs on W₁₈O₄₉ can be traced back to the dangling bonds of the surface W atoms that result from edge-sharing W–O octahedral, which is the basic block in the W₁₈O₄₉ crystal structure (Scheme 1a). As shown in the unit cell of the W₁₈O₄₉ crystal structure (Scheme 1b), SOVs are generated around a 3-fold coordinative O atom (O_{3f}) in the equatorial O of the octahedral located on the edge of the unit cell. Thus, the growth direction along the *b* axis can guarantee the exposure of as many SOVs as possible, as shown in Scheme 1c. In this study, anisotropic W₁₈O₄₉ NWs were synthesized by a template-free approach of the solvothermal. The high-resolution TEM image of a NW is shown in Scheme 1d. The diameter of the NW is approximately 10 nm. The interplanar *d* spacing is approximately 3.79 Å, which is in good agreement with that of the monoclinic W₁₈O₄₉ along the [010] direction (*b* axis).¹⁶ This growth direction is beneficial to the distribution of SOVs on the NW surface, as demonstrated in Scheme 1c. The following XRD pattern further verified that the phase of our NWs is monoclinic W₁₈O₄₉ because all peaks can be assigned according to the Joint Committee on Powder Diffraction Standards Cards (no. 71-2450).

Tungsten oxide NW electrodes with numerous SOVs were prepared by spraying on FTO glass and subsequently sintered at 500 °C in N₂ atmosphere to remove surface impurities. The electrodes were marked as W–O_V–W. The SEM image in Figure 1a clearly shows massive NWs. In situ filling of SOVs in electrodes was conducted at 350 °C temperature in air for 1 h. The color of the W–O_V–W electrode gradually changed from deongaree in the original electrode to gray in the final electrode after SOV filling treatment, as shown in Figure 1. After SOV filling, the electrodes were designated as W–O–W. Increase in treatment temperature converted the tungsten oxide NWs into WO_3 with light yellow color (Figure S1, Supporting Information). The SEM image in Figure 1b notably illustrates the morphology of W–O_V–W after SOV filling. The XRD results in Figure 1c indicate that the NWs maintained the original crystal phase in the bulk. In situ treatment and maintenance of the morphology and crystal phase led to accurate investigation of the effect of SOVs on electrocatalytic activity. In addition, the energy-dispersive X-ray spectroscopy result of W–O_V–W and W–O–W confirmed that the samples only contained W and O elements aside from contaminated carbon (Figure 1d).

To verify the filling of SOVs, XPS was performed to examine the surface chemical state. The full range of the XPS spectra of W–O_V–W and W–O–W is shown in Figure 2a. The peaks were attributed to oxygen and tungsten according to binding energies; no impurities other than contaminated carbon were detected. The photoelectrons from O 1s of W–O_V–W (Figure 2b) displayed a wide and visible asymmetric peak, with the highest point at 530.2 eV. This finding indicated that at least two chemical bonding states, such as O_{2f} and O_{3f}, are on the surface. However, photoelectrons of W–O–W showed a relatively narrow and symmetric peak with a shift to high energy; the highest point was at 530.6 eV. The chemical bonding states tend to show uniform high-energy O_{2f}. The peak at higher photoelectron energy (533.2 eV) may have originated

Scheme 1. (a) WO_6 Octahedron Unit of Saturated Coordinated W in $\text{W}_{18}\text{O}_{49}$;^a (b) Schematic Representation of the Distribution of SOVs inside One $\text{W}_{18}\text{O}_{49}$ Unit Cell;^b (c) Schematic Representation of Exposure of SOVs along b Axis as Many as Possible; (d) We Selectively Synthesized 1D Tungsten Oxide NWs, Growing along the b Axis^c



^aEquatorial O: O_e; apical O: O_a. ^bW_{css} (blue atom) and W_{cus} (green atom) stand for coordinatively saturated sites and coordinatively unsaturated sites of W atom, respectively. O_{2f} (red atom) and O_{3f} (pink atom) stand for one-fold and three-fold coordinative O atom, respectively. ^cCompared with 3D nanostructure, its high aspect ratio is benefitted to expose SOVs in surface of the nanostructure rather than embodied in the bulk.

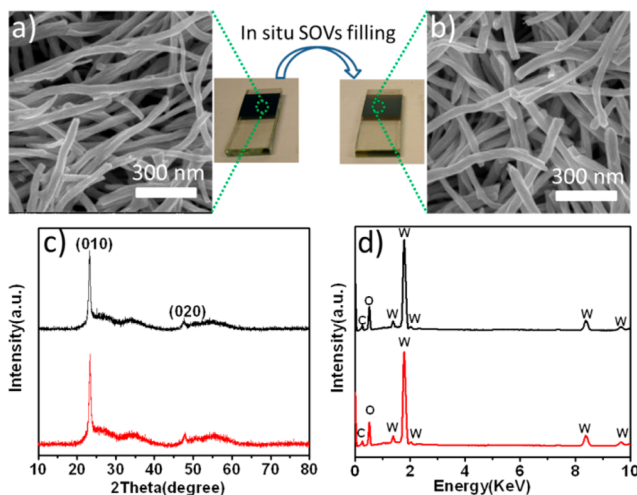


Figure 1. (a, b) SEM of W–O_v–W and W–O–W, respectively; W–O_v–W and W–O–W stand for tungsten oxide electrodes with and without SOVs, respectively. (c, d) XRD and energy-dispersive X-ray spectroscopy for W–O_v–W (black) and W–O–W (red), respectively.

from the residual adsorbed molecules, such as water and/or C–O bond. A complex energy distribution of W 4f photoelectrons was obtained for tungsten, as shown in Figure 2c (black line). The W 4f core-level spectrum could be fit into three couples, which were associated with three different oxidation states of surface W atoms. The main peaks, W 4f $^5/2$ at 37.8 eV and W 4f $^7/2$ at 35.7 eV, were attributed to the 6+ oxidation state of surface W atoms (Figure 2c, red line). The second couple, with lower binding energy at 36.7 and 34.6 eV, was derived from the emission of W 4f $^3/2$ and W 4f $^7/2$ core levels from the five coordination tungsten atoms (Figure 2c, green line). In addition, the third couple, observed at 35.8 and 33.7 eV, corresponded to the unsaturated coordination W⁴⁺ oxidation state (Figure 2c, blue line). These three typical oxidation states have been previously observed in $\text{W}_{18}\text{O}_{49}$ nanomaterial.¹⁰ For the sample obtained after SOV filling treatment (Figure 2d, black line), two steep peaks of W 4f were observed in the spectrum, which is a typical feature of W⁶⁺. No shoulder peak was present in the lower binding energy, indicating that the oxygen vacancies in the NW surface mostly disappeared after SOV filling treatment. Only few W⁵⁺ species were observed. The XPS fitting results (Table S1, Supporting Information) clearly demonstrated that the W⁵⁺/W⁶⁺ ratio of W–O–W (0.041 ± 0.02) is lower than that of W–O_v–W (0.92 ± 0.03). This finding indicates that the oxygen vacancies on the NW surface mostly disappeared after SOV filling treatment, as shown in the schematic of the tungsten oxide surface with and without SOVs (Figure 2e, f). In addition, quantitative determinations of the amount of SOVs were measured at pulse chemisorption mode.¹⁷ Prior to the measurement, the tungsten oxide sample (60 mg) was pretreated with inert gas He flow at 120 °C for 1 h. After heating to 350 °C, the gas flow was switched to oxygen to start O₂ chemisorption. The loop gas was used for each pulse; several pulses were introduced until saturation. As shown in Figure 3a, the intensity of the initial pulse was notably weaker than that of the subsequent pulses, indicating that tungsten oxide prepared in N₂ can significantly adsorb oxygen. However, Figure 3b shows that the intensity of the pulse was nearly unchanged, implying that tungsten oxide hardly adsorbed oxygen after SOV filling treatment. The amount of O₂ was measured with a thermal conductivity

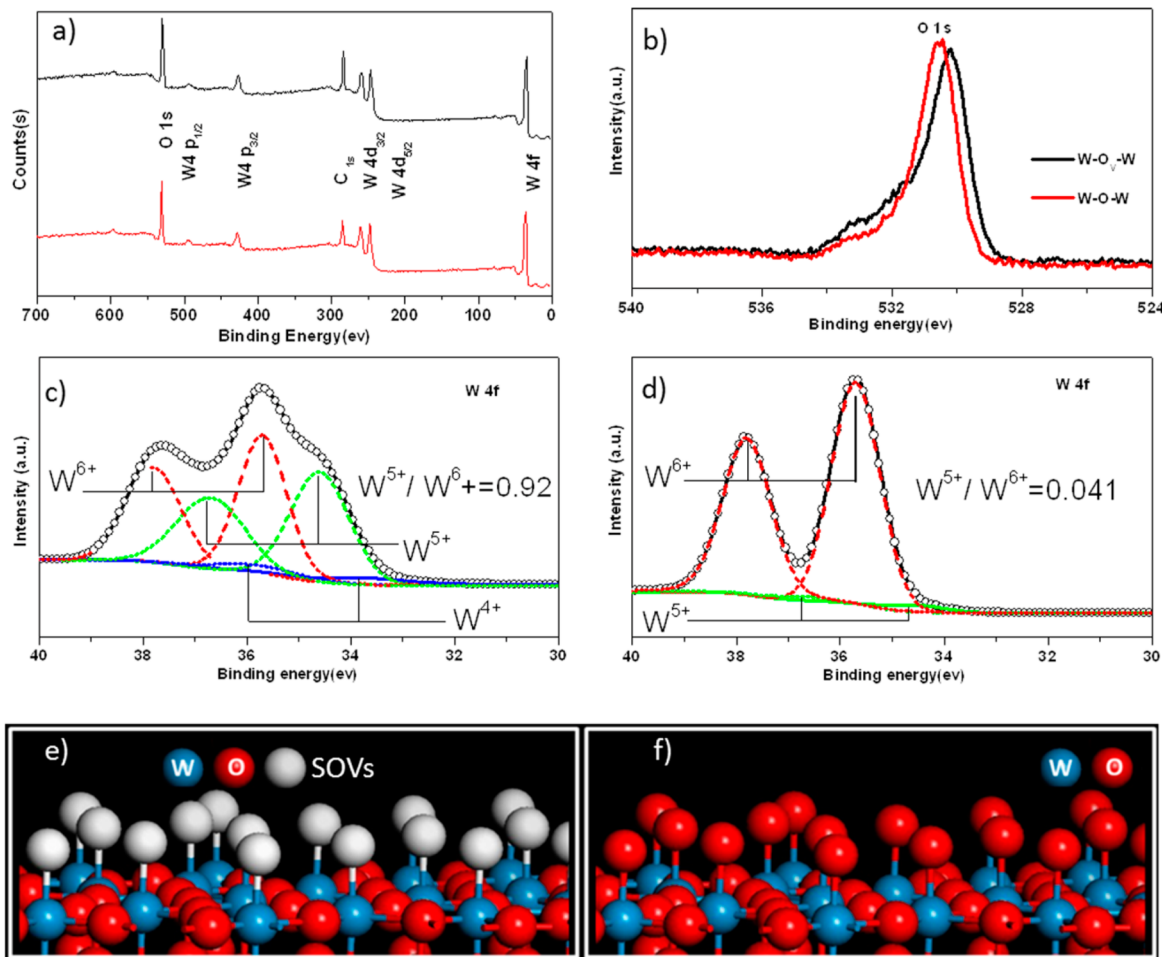


Figure 2. (a) Full-range XPS spectra of W-O_V-W (black) and W-O-W (red). (b) Comparison of O 1s for W-O_V-W (black) and W-O-W (red). O 1s peak of W-O_V-W shows at least two chemical bonding states (O_{2f} and O_{3f}), while that of W-O-W shows mainly one chemical bonding state (O_{2f}). (c, d) W 4f core-level spectra of W-O_V-W and W-O-W, respectively. (e, f) Schematic diagrams of the surface of tungsten oxide with and without SOVs, respectively.

detector, as shown in Figure 3c. The chemical adsorption value of oxygen for W-O_V-W was approximately $20 \pm 0.4 \mu\text{mol g}^{-1}$. This result further confirmed that the oxygen vacancies on the NW surface mostly disappear after SOV filling treatment. The thermal behavior of the samples was studied by thermogravimetric analysis in air atmosphere. There was an obvious weight increment 2% in the W-O_V-W sample when the temperature maintained 350 °C for 1 h (Figure S4, Supporting Information). This may associate with the filling of oxygen vacancies.

The correlation between the quantity of SOVs and the electrocatalytic activity was investigated in an iodine reduction reaction, an important mediator used in clean energy devices, such as electronics, fuel cells, batteries, solar cells, and optical devices.¹⁸ Tungsten oxide samples with different quantities of SOVs were prepared by adjusting the time of SOV filling treatment. The ratio of W⁶⁺ evaluated from XPS increased with increasing oxidation time, showing that the SOV quantity of the samples gradually decreased with increasing oxidation time (Figure 4a; Figure S2 and Table S1, Supporting Information). The effects of SOV quantity on iodine reduction activity were investigated by Tafel polarization using identical electrodes under dark conditions, as shown in Figure 4b. Typically, the Tafel curve comprises three zones.¹⁹ The curve at a very high potential corresponds to the limiting diffusion zone, which is

related to the transport of triiodide and iodide in the electrolyte. The middle potential range (showing a sharp decrease) can be attributed to the Tafel zone, in which the current density of charge transfer appears. The curve at low potential ($|U| < 120 \text{ mV}$) is attributed to the polarization zone. Comparing the Tafel zones in Figure 4b, we can determine that, as the oxidation time increased, the current density exhibited a much slower charge transfer process with the increase in oxidation time, in agreement with the photocurrent density–voltage ($J-V$) curves in solar cells and EIS results. Under the same experimental conditions, the effects of SOV on iodine reduction reaction were characterized through cyclic voltammetry with three electrodes, as shown in Figure S3 (Supporting Information). Two pairs of redox peaks in the cyclic voltammogram for iodide species were observed in Figure S3 (Supporting Information). Pt electrodes exhibit the most reversible and ideally shaped cyclic voltammograms.²⁰ W-O_V-W electrodes also produce reversible voltammograms similar to that of Pt. The voltammetry on W-O-W electrodes is irreversible with large separations of anodic and cathodic peaks ($\Delta E_p = 374 \pm 1 \text{ mV}$), clearly illustrating a distinctly inferior catalytic activity compared with that of W-O_V-W.

DSCs were assembled using a I^-/I_3^- redox mediator system to investigate further the effect of catalyst SOVs on the performance of the photovoltaic device.²¹ $J-V$ curves were

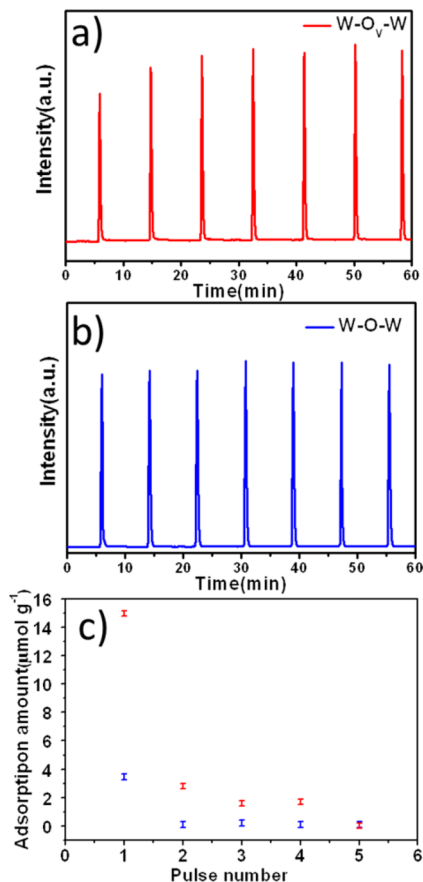


Figure 3. (a, b) Oxygen pulse chemisorption of W–O_v–W and W–O–W, respectively. (c) Adsorption amount–pulse number curves of W–O_v–W (red) and W–O–W (blue), which is measured by thermal conductivity detector.

obtained for these DSCs based on the samples with different oxidation times and Pt under AM 1.5, 100 mW cm⁻² simulated illumination, as shown in Figure 4c. The detailed photovoltaic parameters are summarized in Table 1. The DSCs based on W–O_v–W produced photoelectric conversion efficiencies (PCEs) of (7.8 ± 0.1)% , which is close to that of DSCs based on Pt electrodes. A significant reduction in fill factor (from 0.70 ± 0.01 to 0.54 ± 0.01) of the DSCs resulted in a relatively low PCE of (5.6 ± 0.01)% as the oxidation time increased. The distinctive decrease of PCEs after SOV filling treatment indicated that SOVs in counter electrodes affect the property of the photovoltaic devices.

EIS values were measured using identical counter electrodes under dark conditions to compare quantitatively the resistance of catalytic activity in catalysts.^{22,23} According to an equivalent circuit diagram (Figure 5a), the EIS results shown in Figure 5b, c were fitted by “Z-view” software.^{19,24} The fitting results of Nyquist plots listed in Table 1 indicated that series resistance (R_s) values for samples with different filling times were nearly the same but higher than that of Pt. The charge transfer resistance (R_{ct}) of (1.1 ± 0.1) Ω for W–O_v–W was smaller than that of (3.7 ± 0.4) Ω for Pt. R_{ct} immensely increased from (1.1 ± 0.1) to (77.8 ± 0.3) Ω with the increase in oxidation time, causing an increase in Nernst diffusion impedance (Z_N). Catalytic activity sites declined after lowering the SOV quantity. Thus, all the electrocatalytic results clearly revealed that iodide reduction reaction activity is notably dependent on tungsten

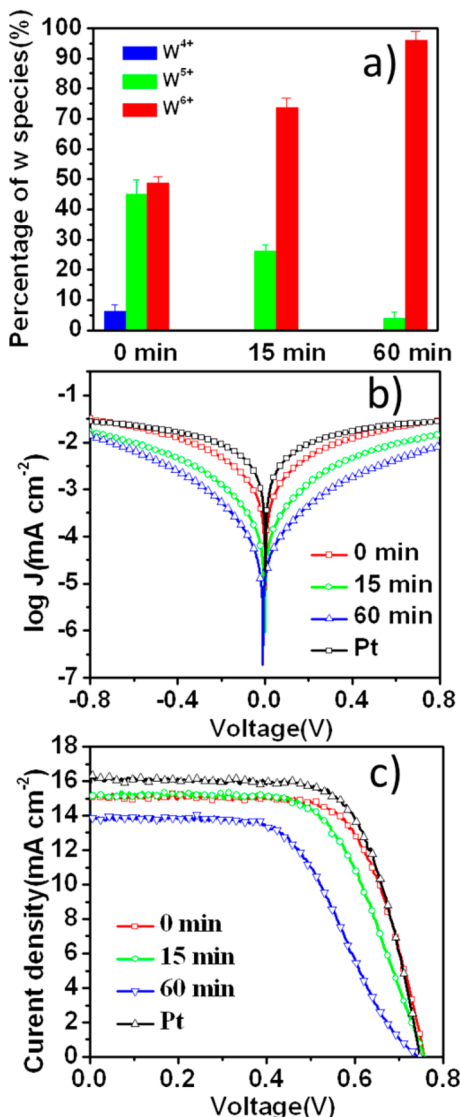


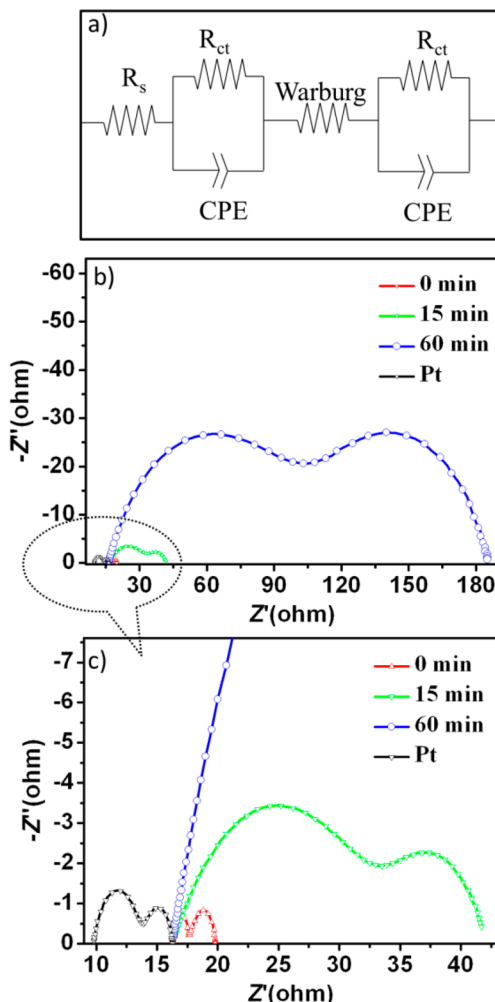
Figure 4. (a) Percentage of W species on the surface of samples with different filling SOVs time. (b) Tafel curves measured by the two identical catalytic electrodes based on the samples with different filling SOVs time. (c) Photocurrent density–voltage curves of DSCs utilizing I[−]/I₃[−] as the redox mediator.

oxide catalyst SOVs, which serve as important catalytic site descriptors.

The mechanism of SOVs as important catalytic sites is summarized as follows. The mechanism comprises six important steps, as shown in Scheme 2. The diffusion of an iodine molecule is typically rapid and in equilibrium.²⁵ The exact mechanism for the iodine reduction reaction is unclear; however, previous studies have shown that the iodine molecule is preferentially adsorbed in the presence of the metal atoms in an inorganic complex rather than in the presence of nonmetallic atoms.^{26–28} Thus, iodine molecules should be on top of W atoms. SOVs on tungsten oxides surface are preferential adsorption sites for iodine molecules (I₂(sol) + SOVs ↔ I₂(SOVs)). Upon adsorption at the tungsten oxide surface, the iodine molecule can readily dissociate into two iodine atoms (I₂(SOVs) + 2e[−] ↔ 2I[−](sol) + SOVs)).

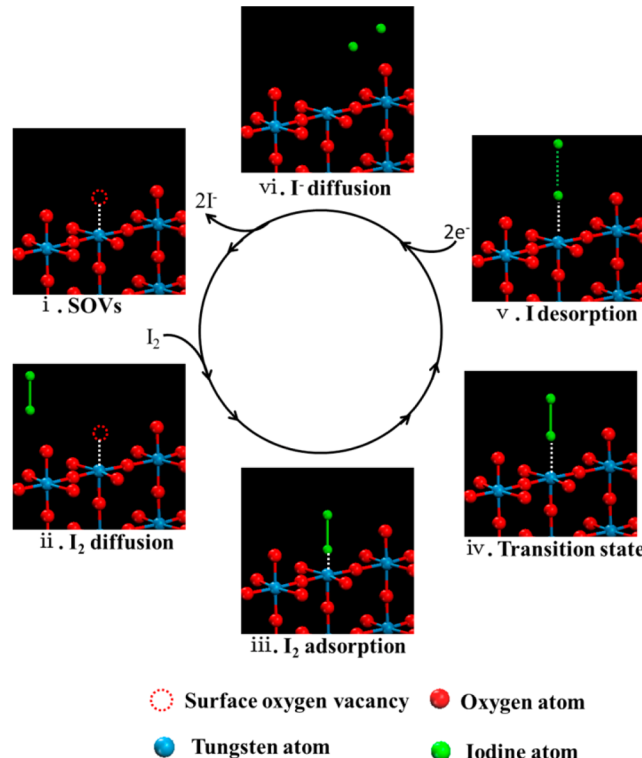
Table 1. Photovoltaic and Electrochemical Parameters Based on the Samples with Different Times of Filling SOVs, Utilizing I⁻/I₃⁻ as the Redox Mediator

time of filling SOVs	V _{oc} (V)	J _{sc} (mA cm ⁻²)	FF	PCEs (%)	R _s (Ω)	R _{ct} (Ω)	Z _N (Ω)
0 min	0.75 ± 0.01	14.96 ± 0.1	0.70 ± 0.01	7.8 ± 0.1	16.33 ± 0.04	1.1 ± 0.1	2.3 ± 0.4
15 min	0.75 ± 0.01	14.92 ± 0.06	0.64 ± 0.01	7.2 ± 0.12	16.30 ± 0.01	15.9 ± 0.2	9.9 ± 0.1
60 min	0.74 ± 0.01	13.94 ± 0.14	0.54 ± 0.01	5.6 ± 0.01	16.28 ± 0.03	77.8 ± 0.3	91.5 ± 0.2
Pt	0.74 ± 0.01	15.61 ± 0.20	0.70 ± 0.03	8.1 ± 0.2	9.76 ± 0.01	3.7 ± 0.4	2.7 ± 0.3

**Figure 5.** (a) Equivalent circuit diagram for symmetrical cells fabricated with two identical counter electrodes. (b) Nyquist plots measured by the two identical electrodes based on samples with different filling SOVs time. (c) Nyquist plots displayed at different ranges.

4. CONCLUSIONS

In summary, we identified SOV-dependent electrocatalytic activity for energy conversion. 1D tungsten oxide NWs with numerous SOVs were synthesized by clarifying the origin of SOVs and their distribution. Compared with a 3D nanostructure, NWs with high aspect ratio can expose SOVs on the surface of the nanostructure rather than embody them in the bulk. Through in situ SOV filling in the electrodes, the crystal phase and morphology of NWs were maintained, and the link between SOVs of tungsten oxide catalyst and catalytic activity was clearly identified. The surface chemical and electrocatalytic results clearly revealed that iodide reduction reaction activity was notably dependent on tungsten oxide catalyst SOVs, which

Scheme 2. Schematic Mechanism of SOVs as an Important Catalytic Site for Electrocatalysis

serve as important catalytic site descriptors. These findings may clarify the fundamental features of SOVs on metal oxides and contribute to the rational design of efficient catalysts and supports.

ASSOCIATED CONTENT

Supporting Information

XRD pattern of tungsten oxide NWs; W 4f core-level spectra; cyclic voltammograms; XPS fitting results; TGA patterns; schematics of typical circuit diagrams; and EIS plots. This material is available free of charge via the Internet at <http://pubs.acs.org>.

AUTHOR INFORMATION

Corresponding Author

*E-mail: tinglima@dlut.edu.cn.

Notes

The authors declare no competing financial interest.

ACKNOWLEDGMENTS

This work was financially supported by National Natural Science Foundation of China (grant nos. 51273032 and 91333104), International Science & Technology Cooperation Program of China (grant no. 2013DFAS1000).

■ REFERENCES

- (1) Esch, F.; Fabris, S.; Zhou, L.; Montini, T.; Africh, C.; Fornasiero, P.; Comelli, G.; Rosei, R. Electron localization determines defect formation on ceria substrates. *Science* **2005**, *309*, 752–755.
- (2) Over, H. Surface chemistry of ruthenium dioxide in heterogeneous catalysis and electrocatalysis: From fundamental to applied research. *Chem. Rev.* **2012**, *112*, 3356–3426.
- (3) Schaub, R.; Wahlstrom, E.; Ronnau, A.; Laegsgaard, E.; Stensgaard, I.; Besenbacher, F. Oxygen-mediated diffusion of oxygen vacancies on the $\text{TiO}_2(110)$ surface. *Science* **2003**, *299*, 377–379.
- (4) Schaub, R. Oxygen-mediated diffusion of oxygen vacancies on the $\text{TiO}_2(110)$ surface. *Science* **2006**, *314*, 925–925.
- (5) Fu, Q.; Saltsburg, H.; Flytzani-Stephanopoulos, M. Active nonmetallic Au and Pt species on ceria-based water-gas shift catalysts. *Science* **2003**, *301*, 935–938.
- (6) Liu, Z. P.; Jenkins, S. J.; King, D. A. Origin and activity of oxidized gold in water-gas-shift catalysis. *Phys. Rev. Lett.* **2005**, *94*, 196102–196106.
- (7) Lin, J.; Huang, Y.; Li, L.; Wang, A.; Zhang, W.; Wang, X.; Zhang, T. Activation of an Ir-in-CeO₂ catalyst by pulses of CO: The role of oxygen vacancy and carbonates in CO oxidation. *Catal. Today* **2012**, *180*, 155–160.
- (8) Qiao, B.; Wang, A.; Yang, X.; Allard, L. F.; Jiang, Z.; Cui, Y.; Liu, J.; Li, J.; Zhang, T. Single-atom catalysis of CO oxidation using Pt₁/FeO_x. *Nat. Chem.* **2011**, *3*, 634–641.
- (9) Henderson, M. A.; White, J. M.; Uetsuka, H.; Onishi, H. Photochemical charge transfer and trapping at the interface between an organic adlayer and an oxide semiconductor. *J. Am. Chem. Soc.* **2003**, *125*, 14974–14975.
- (10) Manthiram, K.; Alivisatos, A. P. Tunable localized surface plasmon resonances in tungsten oxide nanocrystals. *J. Am. Chem. Soc.* **2012**, *134*, 3995–3998.
- (11) Zheng, H.; Ou, J. Z.; Strano, M. S.; Kaner, R. B.; Mitchell, A.; Kalantar-zadeh, K. Nanostructured tungsten oxide – Properties, synthesis, and applications. *Adv. Funct. Mater.* **2011**, *21*, 2175–2196.
- (12) Yella, A.; Tahir, M. N.; Meuer, S.; Zentel, R.; Berger, R.; Panthofer, M.; Tremel, W. Synthesis, characterization, and hierarchical organization of tungsten oxide nanorods: Spreading driven by Marangoni flow. *J. Am. Chem. Soc.* **2009**, *131*, 17566–17575.
- (13) Xi, G.; Ye, J.; Ma, Q.; Su, N.; Bai, H.; Wang, C. In situ growth of metal particles on 3D urchin-like WO₃ nanostructures. *J. Am. Chem. Soc.* **2012**, *134*, 6508–6511.
- (14) Xi, G.; Ouyang, S.; Li, P.; Ye, J.; Ma, Q.; Su, N.; Bai, H.; Wang, C. Ultrathin W₁₈O₄₉ nanowires with diameters below 1 nm: Synthesis, near-infrared absorption, photoluminescence, and photochemical reduction of carbon dioxide. *Angew. Chem., Int. Ed.* **2012**, *51*, 2395–2399.
- (15) Zhou, H.; Shi, Y.; Wang, L.; Zhang, H.; Zhao, C.; Hagfeldt, A.; Ma, T. Notable catalytic activity of oxygen-vacancy-rich WO_{2.72} nanorod bundles as counter electrodes for dye-sensitized solar cells. *Chem. Commun.* **2013**, *49*, 7626–7628.
- (16) Guo, C.; Yin, S.; Yan, M.; Kobayashi, M.; Kakihana, M.; Sato, T. Morphology-controlled synthesis of W₁₈O₄₉ nanostructures and their near-infrared absorption properties. *Inorg. Chem.* **2012**, *51*, 4763–4771.
- (17) Wei, X.; Yang, X.-F.; Wang, A.-Q.; Li, L.; Liu, X.-Y.; Zhang, T.; Mou, C.-Y.; Li, J. Bimetallic Au-Pd alloy catalysts for N₂O decomposition: Effects of surface structures on catalytic activity. *J. Phys. Chem. C* **2012**, *116*, 6222–6232.
- (18) Svensson, P. H.; Kloo, L. Synthesis, structure, and bonding in polyiodide and metal iodide-iodine systems. *Chem. Rev.* **2003**, *103*, 1649–1684.
- (19) Wang, Q.; Moser, J. E.; Gratzel, M. Electrochemical impedance spectroscopic analysis of dye-sensitized solar cells. *J. Phys. Chem. B* **2005**, *109*, 14945–14953.
- (20) Zhou, H.; Shi, Y.; Qin, D.; An, J.; Chu, L.; Wang, C.; Wang, Y.; Guo, W.; Wang, L.; Ma, T. Printable fabrication of Pt-and-ITO free counter electrodes for completely flexible quasi-solid dye-sensitized solar cells. *J. Mater. Chem. A* **2013**, *1*, 3932–3937.
- (21) Oregan, B.; Gratzel, M. A low-cost, high-efficiency solar-cell based on dye-sensitized colloidal TiO₂ film. *Nature* **1991**, *353*, 737–740.
- (22) Wang, M. K.; Anghel, A. M.; Marsan, B.; Ha, N. L. C.; Pootrakulchote, N.; Zakeeruddin, S. M.; Gratzel, M. CoS Supersedes Pt as efficient electrocatalyst for triiodide reduction in dye-sensitized solar cells. *J. Am. Chem. Soc.* **2009**, *131*, 15976–15977.
- (23) Bisquert, J.; Graetzel, M.; Wang, Q.; Fabregat-Santiago, F. Three-channel transmission line impedance model for mesoscopic oxide electrodes functionalized with a conductive coating. *J. Phys. Chem. B* **2006**, *110*, 11284–11290.
- (24) Sun, H.; Qin, D.; Huang, S.; Guo, X.; Li, D.; Luo, Y.; Meng, Q. Dye-sensitized solar cells with NiS counter electrodes electrodeposited by a potential reversal technique. *Energy Environ. Sci.* **2011**, *4*, 2630–2637.
- (25) Hauch, A.; Georg, A. Diffusion in the electrolyte and charge-transfer reaction at the platinum electrode in dye-sensitized solar cells. *Electrochim. Acta* **2001**, *46*, 3457–3466.
- (26) Hou, Y.; Wang, D.; Hua Yang, X.; Qi Fang, W.; Zhang, B.; Feng Wang, H.; Zhong Lu, G.; Hu, P.; Jun Zhao, H.; Gui Yang, H. Rational screening low-cost counter electrodes for dye-sensitized solar cells. *Nat. Commun.* **2013**, *4*, 1583–1583.
- (27) Sining, Y.; Hong, Z.; Huihai, P.; Junhong, C.; Hagfeldt, A.; Tingli, M. Metal oxide/carbide/carbon nanocomposites: In situ synthesis, characterization, calculation, and their application as an efficient counter electrode catalyst for dye-sensitized solar cells. *Adv. Energy Mater.* **2013**, *3*, 1407–1412.
- (28) Wang, Y.-C.; Wang, D.-Y.; Jiang, Y.-T.; Chen, H.-A.; Chen, C.-C.; Ho, K.-C.; Chou, H.-L.; Chen, C.-W. FeS₂ nanocrystal ink as a catalytic electrode for dye-sensitized solar cells. *Angew. Chem., Int. Ed.* **2013**, *52*, 6694–6698.